IJMMM International Journal of Minerals, Metallurgy and Materials 矿物冶金与材料学报（英文版）

Effects of iron oxide on crystallization behavior and spatial distribution of spinel in stainless steel slag

Zihang Yan, Qing Zhao, Chengzhi Han, Xiaohui Mei, Chengjun Liu, and Maofa Jiang

Cite this article as:
Zihang Yan, Qing Zhao, Chengzhi Han, Xiaohui Mei, Chengjun Liu, and Maofa Jiang, Effects of iron oxide on crystallization behavior and spatial distribution of spinel in stainless steel slag, *Int. J. Miner. Metall. Mater.*, (2024). https://doi.org/10.1007/s12613-023-2713-7

INTERNATIONAL JOURNAL OF
Minerals, Metallurgy and Materials

Volume 31, Number 2, February 2024
Page 292

Research Article https://doi.org/10.1007/s12613-023-2713-7

Effects of iron oxide on crystallization behavior and spatial distribution of spinel in stainless steel slag

Zihang Yan[1,2], *Qing Zhao*[1,2)✉], *Chengzhi Han*[1,2)], *Xiaohui Mei*[1,2)], *Chengjun Liu*[1,2)], *and Maofa Jiang*[1,2)]

1) Key Laboratory for Ecological Metallurgy of Multimetallic Mineral (Ministry of Education), Northeastern University, Shenyang 110819, China
2) School of Metallurgy, Northeastern University, Shenyang 110819, China
(Received: 2 March 2023; revised: 20 July 2023; accepted: 21 July 2023)

Abstract: Chromium plays a vital role in stainless steel due to its ability to improve the corrosion resistance of the latter. However, the release of chromium from stainless steel slag (SSS) during SSS stockpiling causes detrimental environmental issues. To prevent chromium pollution, the effects of iron oxide on crystallization behavior and spatial distribution of spinel were investigated in this work. The results revealed that FeO was more conducive to the growth of spinels compared with Fe_2O_3 and Fe_3O_4. Spinels were found to be mainly distributed at the top and bottom of slag. The amount of spinel phase at the bottom decreased with the increasing FeO content, while that at the top increased. The average particle size of spinel in the slag with 18wt% FeO content was 12.8 μm. Meanwhile, no notable structural changes were observed with a further increase in FeO content. In other words, the spatial distribution of spinel changed when the content of iron oxide varied in the range of 8wt% to 18wt%. Finally, less spinel was found at the bottom of slag with a FeO content of 23wt%.

Keywords: stainless steel slag; spinel; chromium; waste remediation; ferrous oxide

1. Introduction

Stainless steel (SS) industry in China has rapidly developed in recent decades, accounting for more than half of the global output. Meanwhile, the steady growth of SS is accompanied by a huge release of stainless steel slag (SSS), which is one third of that of SS [1]. As an essential element in SS smelting, chromium is also detected in SSS [2]. The main composition of SSS produced by electric arc furnace (EAF) smelting includes CaO and MgO (40wt%–50wt%), SiO_2 (20wt%–30wt%), MnO (2wt%–3wt%), Al_2O_3 (5wt%–10wt%), FeO (8wt%–22wt%), and Cr_2O_3 (2wt%–10wt%); moreover, the weight ratio of CaO and SiO_2 (w(CaO)/w(SiO_2)) in the SSS structure is kept at a level of ≤2.5. The naturally cooled EAF slag has a black color along with a coarse particle composition and properties closer to those of the common steel slag, where the elements with a mass fraction greater than 1wt% are Ca, Mg, Si, Al, Fe, Cr, O, etc. [3]. At the end of smelting, chromium in the SSS is mainly found in Cr^{2+} or Cr^{3+} state [4]. During treatment and storage, the chromium oxide in the slag is readily oxidized to hexavalent chromium [5]. Hexavalent chromium is toxic, unstable, and easy to release from slag, which can cause serious harm to human health and the environment [6–7]. Therefore, to realize the resource utilization of SSS, searching for approaches to effectively solve issues associated with chromium slag pollution has become an urgent task.

In the current study, a large amount of chromium in SSS has been enriched in a stable spinel phase [8–9]. Moreover, the addition of iron oxide exerted the even better effect on the formation and growth of spinel phase [10]. The recovery of chromium can also be realized via magnetic separation of SSS [11–12], and introducing the iron oxide makes the process more convenient. However, the impact of magnetic separation can be greatly affected by the presence of an excessive silicate phase in the slag [13–14]. Some scholars [15–16] have found that the spinel phase can be localized within certain regions of slag, which can significantly improve the chromium recovery efficiency. During the production, these specific areas in the SSS can be purposely treated so that the spinel-enriched part can be separated from the whole slag and spinel can further be recovered via magnetic separation [17–18]. Most residual slag is chromium-free and can be used as ordinary steel slag for building materials, carbon dioxide capture, and so on [19]. Combined with the spatial distribution of various phases in SSS, it has a significant impact on the recovery of chromium and is conducive to the treatment and utilization of SSS.

In the present study, the fugitive behavior of chromium and the crystallization features of spinel in SSS were systematically analyzed, and the melt reforming treatment was performed to promote the enrichment of a stable spinel phase with chromium and the precipitation of a large amount of spinel phase in the target area [20]. It was shown that adding the iron oxide could not only increase the size of the spinel particles, but also facilitate the subsequent magnetic separa-

✉ Corresponding author: Qing Zhao E-mail: zhaoq@smm.neu.edu.cn

tion and recovery of chromium-containing spinel phases in SSS. Based on the spatial distribution of spinel phases in SSS, directional recovery of chromium and recycling of SSS were realized as well [21].

2. Experimental

Fine reagent-grade powders, namely, CaO, SiO_2, MgO, MnO, Al_2O_3, $FeC_2O_4{\cdot}2H_2O$, Cr_2O_3, Fe_2O_3, and Fe_3O_4, were taken as raw materials. Among them, $FeC_2O_4{\cdot}2H_2O$ was used to replace FeO. The experimental slag samples were prepared from the above reagents with the compositions close to the EAF slag generated from stainless steelmaking, as shown in Table 1. The degree of basicity of the slags was 1.5 and the content of Cr_2O_3 therein was 5wt%. To explore the effect of different iron oxides on SSS, 10wt% FeO as S2, 10wt% Fe_2O_3 as S3, and 10wt% Fe_3O_4 as S4 were added to the experimental slag sample S1. Besides, to elucidate the influence of different amounts of FeO on SSS, FeO dopant (5wt%, 10wt%, and 15wt%) was added to the experimental slag S1 (the corresponding specimens were referred to as S5, S2, and S6, respectively).

Table 1. Chemical compositions of experimental slag samples

Sample No.	Chemical composition / wt%									*R*
	Fe_2O_3	Fe_3O_4	CaO	SiO_2	MgO	MnO	Al_2O_3	FeO	Cr_2O_3	
S1	—	—	40.80	27.20	10.00	3.00	6.00	8.00	5.00	1.5
S2	—	—	40.80	27.20	10.00	3.00	6.00	18.00	5.00	1.5
S3	10.00	—	40.80	27.20	10.00	3.00	6.00	8.00	5.00	1.5
S4	—	10.00	40.80	27.20	10.00	3.00	6.00	8.00	5.00	1.5
S5	—	—	40.80	27.20	10.00	3.00	6.00	13.00	5.00	1.5
S6	—	—	40.80	27.20	10.00	3.00	6.00	23.00	5.00	1.5

Note: *R* refers to the degree of alkalinity.

After accurate weighing and thorough homogenization, 5 g of each slag sample was put in the MgO crucible, which was then placed in the high-temperature quenching furnace for subsequent heating to 1600°C in an argon atmosphere (see Fig. S1(a)). The temperature was kept for 60 min to ensure that slags were completely melted. In this experiment, two different cooling modes were used to explore the changes in SSS. The first consisted in direct quenching of slags after holding them at 1600°C for 60 min. The second was the slow cooling of slags down to 1300°C at a cooling rate of 3.5°C/min after 60 min of heating at 1600°C [22], followed by water quenching.

Furthermore, in order to study the effect of FeO on SSS, 2 g of FeO reagent was pressed into a block. Then, 30 g of evenly mixed S1 slag was poured into the MgO crucible, which was then placed in the graphite crucible, and both were put together into the high-temperature tube furnace, as shown in Fig. S1(b). Argon was introduced during the experiment to provide an inert atmosphere. The slags were heated to 1600°C and held at this temperature for 60 min to ensure their complete melting. Finally, the prepared FeO blocks were immersed in the melts and held at 1600°C for 1 min, and slags were then quickly removed from the furnace, quenched in water, and separated from the MgO crucible.

The morphologies of synthesized samples were characterized by a scanning electron microscope (SEM, Jeol 6480LV) coupled with a Thermo Electron NSS energy-dispersive spectrometer (EDS). The phase compositions of slags were analyzed using a Philips X'Pert X-ray diffractometer (XRD) equipped with a Cu K_α radiation source (λ = 0.15418 nm). The XRD profiles were acquired in the range of $10° \le 2\theta \le 80°$ at a step of 0.008° and processed using Powder Diffraction File databases (the International Center for Diffraction Data) embedded in the Xert High score software. The elemental valence states were determined via X-ray photoelectron spectroscopy (XPS, Thermo Scientific K-Alpha). The sizes of the spinel crystals were evaluated from the SEM images using Image-Pro Plus 6.0 (IPP 6.0) software. For this purpose, spinel phases were selected in 64 different fields of view under 1000× magnification, and the average diameter ($\overline{D}$) of spinel particles was then determined as follows:

$$\overline{D} = \frac{1}{n}\sum_{i=1}^{n} D_i \tag{1}$$

where n is the number of spinel particles over all fields of view, and D_i is the diameter of the ith spinel particle (μm) depending on its area S (μm^2) as

$$D = \sqrt{\frac{4S}{\pi}} \tag{2}$$

More details about the calculation method can be found in the previous study [23].

In addition, to investigate the spatial distribution of the spinel phase in the SSS melt, the crucible containing the slag sample after water quenching was cut into small pieces, which were then exposed to a series of grinding and polishing procedures for the SEM observation. Meanwhile, because of the limited field of view in the SEM, an image stitching software was applied to splice the SEM images and to obtain a relatively complete spatial distribution map of the phases composing the slag.

3. Results and discussion

3.1. Effect of iron oxide composition on SSS

The microstructures of the samples without iron oxides

and those with 10wt% FeO, 10wt% Fe_2O_3, and 10wt% Fe_3O_4 are shown in Fig. 1. The mineral structures and sizes of spinel crystals are presented in Fig. 1(a)–(d), whereas other phases can be clearly distinguished in Fig. 1(e)–(h). As seen in Fig. 1, the SSS sample consisted of four different mineral phases. According to EDS analysis, the white particles with regular quadrilateral or pentagonal shapes were attributed to spinel crystals [24–25] ((Mg, Fe)(Cr, Fe, Al)$_2O_4$). The white droplet inclusions with irregular edges and corners revealed the presence of RO (generally referring to FeO, MgO, and MnO phases and their solid solutions) phase. The gray matrix phase was assigned to merwinite ($Ca_3MgSi_2O_8$), and the light gray ribbons were ascribed to a glass phase. The specific composition of each phase is given in Table 2. According to the data, the increase of Fe content in the RO phase was mainly due to the increase of total iron content in the slag after the addition of iron oxide. Meanwhile, the iron content in the spinel phase increased because Fe^{2+} and Fe^{3+} in the slag entered the spinel phase in a similar manner [26], which promoted the growth of spinel particles. The same phenomenon was also observed by Zeng *et al.* [27].

By comparing Fig. 1(a)–(d) and Fig. 1(e)–(h), it was obvious that more spinel phases in the form of dense aggregates existed in the field of view of Fig. 1(a)–(d). In Fig. 1(e)–(h), fewer spinel phases were present, and even no spinel phase was found. However, there were abundant RO, glass and merwinite phases in the field of view. Since the same situation was observed for all four groups of slags, this was the evidence of some regularity in phase compositions of those specimens. In Fig. 1(e), the spinel phase was mainly concen-

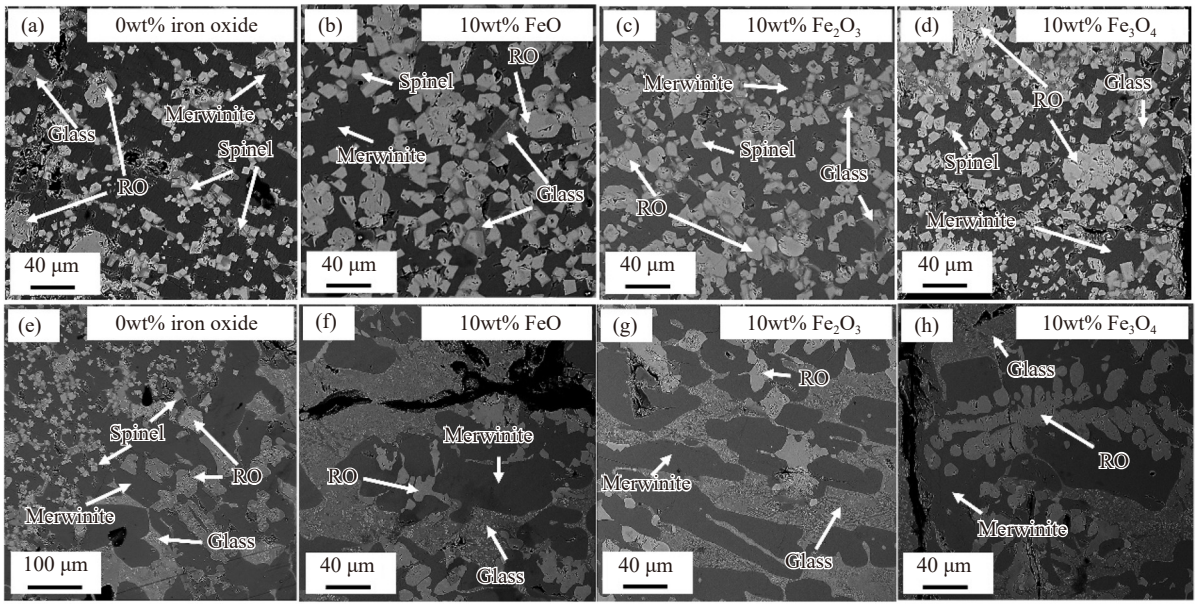

Fig. 1. SEM images of experimental slag samples with different iron oxides: (a, e) 0wt% iron oxide; (b, f) 10wt% FeO; (c, g) 10wt% Fe_2O_3; (d, h) 10wt% Fe_3O_4.

Table 2. EDS results on each phase in Fig. 1 at%

Figure No.	Phase	Ca	Si	Mg	Mn	Al	Fe	Cr	O
Fig. 1(a) and (e)	Merwinite	20.09	15.57	7.54	—	—	—	—	56.80
	Spinel	—	—	11.91	—	4.78	5.71	14.22	63.38
	Glass	13.40	10.72	6.48	1.81	4.15	6.20	—	57.24
	RO	—	—	32.37	2.64	—	11.98	—	53.01
Fig. 1(b) and (f)	Merwinite	21.32	14.40	7.63	—	—	—	—	56.65
	Spinel	—	—	10.88	—	3.88	8.23	12.70	64.31
	Glass	10.66	8.31	5.96	1.18	4.77	7.93	—	61.19
	RO	—	—	24.23	1.55	—	16.43	—	57.79
Fig. 1(c) and (g)	Merwinite	20.43	13.78	6.62	—	—	—	—	59.17
	Spinel	—	—	10.50	—	3.96	8.85	12.23	64.46
	Glass	11.69	10.35	4.59	1.48	5.42	7.00	—	59.47
	RO	—	—	23.25	1.92	—	16.07	—	58.76
Fig. 1(d) and (h)	Merwinite	22.16	14.02	7.21	—	—	—	—	56.61
	Spinel	—	—	10.06	—	4.11	8.12	12.25	65.45
	Glass	12.32	9.91	5.78	1.17	4.47	7.17	—	59.17
	RO	—	—	23.37	2.15	—	17.68	—	56.80

trated in the upper left corner of the image, and there was a well-defined boundary, indicating a spatial distribution of various phases in the SSS melt. The identical picture was also reported by Wang and Sohn [28] in the case of SSS with MnO additive. Such a phase distribution in the SSS exerted a positive impact on the harmless treatment of the slag, as well as on the recovery and utilization of chromium resources [29].

Since the spinel grain size ≤ 6 μm [30], the crystal development was incomplete and was accompanied by the emergence of lattice defects and impurity elements, which affected the stability of the spinel. It is noteworthy that the larger the spinel size, the easier the valuable elements can be recovered by magnetic separation, which is beneficial for structural stabilization of the slag [31]. It can be clearly seen from Fig. 1(a)–(d) that the grain size of the spinel phase precipitated in the slag with 10wt% FeO doping was significantly larger than that in other slag samples. Therefore, the average particle size of the spinel phase was further measured and calculated to assess the effect of different iron oxides on the spinel production in SSS. The influence of different iron oxides on the particle size of the spinel is shown in Fig. 2. According to the plots, the maximum average particle size of the spinel was 12.8 μm at the maximum size of 31.05 μm, which was achieved in the slag sample with 10wt% FeO content. The minimum average particle size of 7.7 μm was obtained for the iron-oxide free slag, and the maximum size in this specimen was 18.9 μm, which was also smaller than those of other slag samples with iron oxide additives. The average and maximum particle sizes of the slags with 10wt% Fe_2O_3 and 10wt% Fe_3O_4 dopant contents were almost close to each other. Therefore, both types of oxides had the similar effects on the spinel phases in the slags.

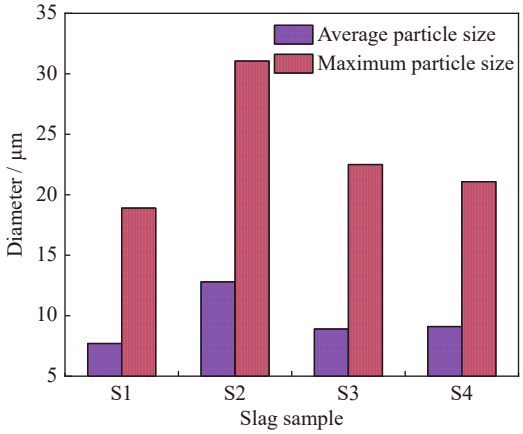

Fig. 2. Effect of different iron oxides on spinel particle size.

In summary, three kinds of iron oxides promoted the development of spinel crystals. At the same time, the impact of FeO addition on the spinel phase was more pronounced than those enriched by introducing Fe_2O_3 and Fe_3O_4 or even in the absence of iron oxide. Therefore, the presence of FeO was more conducive to the subsequent processing and utilization of SSS [32].

The XRD analysis was then performed on the samples quenched with different iron oxides, and the results are depicted in Fig. 3. The highest XRD peak near 34° was attributed to merwinite as the major mineral phase in the slags, which agreed with the above SEM–EDS data. The emergence of XRD peaks associated with spinel phases was the evidence of spinel crystal precipitates in all samples. Besides, with the addition of iron oxides, the diffraction peak intensity of merwinite gradually decreased, especially in the case of FeO and Fe_2O_3. This meant that the presence of iron oxide in the slag structure could have inhibited the precipitation of merwinite.

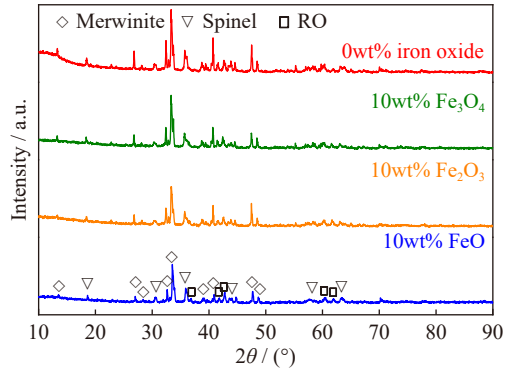

Fig. 3. XRD patterns of slag samples with different iron oxides.

3.2. Effect of FeO addition on crystallization behavior of spinel

Fig. 4 displays the microstructures of the samples with different amounts of FeO. In order to observe the spatial distribution of each phase in the slag sample in a clearer manner, several SEM images with a small field of view were spliced into the long photos from the top to the bottom of the crucible, as shown in Fig. 4(a)–(d). Combined with the EDS data, the SEM results highlighted the presence of four main phases: spinel, glass phase, merwinite, and RO phase.

A visual inspection of Fig. 4 from top to bottom revealed the same regularity for all four slag samples; that is, the phases in the SSS were spatially distributed in the melt, and

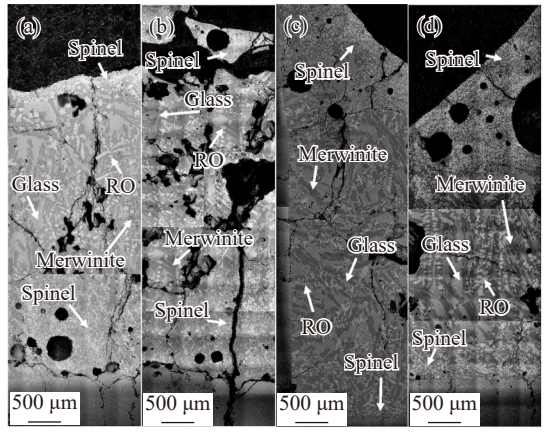

Fig. 4. SEM images of spliced slag samples with different FeO contents at 1300°C: (a) 8wt%, (b) 13wt%, (c) 18wt%, and (d) 23wt%.

abundant spinel phases were precipitated at the top and bottom of the slags. It is noteworthy that no spinel has been detected in the middle part of the slags. The matrix phase in the whole picture was ascribed to the merwinite phase, and a large amount of glass and RO phases was distributed in the middle of the slag. On the other hand, a comparative analysis of Fig. 4(a)–(d) disclosed that adding 8wt% FeO (Fig. 4(a)) resulted in plenty of spinel phase precipitates at the bottom and their scarceness at the top of the crucible. With the continuous addition of FeO, the amount of the spinel phase at the bottom gradually decreased, while that at the top gently increased. However, this process was not continuous. As shown in Fig. 4(c), at the FeO content of 18wt%, the spinel phase accumulated at the top rather than at the bottom of the slag. At this time, the amount of spinel at the bottom of the slag was lower than those in the other three slags. According to Fig. 4(d), the content of spinel phase at the bottom of the slag with 23wt% FeO content increased relative to that at 18wt% FeO content, while the total quantity of spinel was still inferior to the slags with 8wt% and 13wt% FeO doping.

In view of this specific spinel phase distribution at the top and bottom of the slag, the next step of the research is aimed at verifying whether the precipitation of the spinel phase is not caused by heat conduction and rapid cooling at the edge during water quenching. In Fig. 4(c), no spinel phase was found on the side wall of the crucible in contact with water, thereby proving the above assumption.

To sum up, each phase in the SSS exhibited its particular spatial distribution (see Fig. 5). Adding the appropriate amount of FeO changed the distribution of the spinel phase and made it aggregate at the top of the slag. Among the four different slags, the specimen with 18wt% FeO doping contained the smallest amount of spinel at the bottom, while presenting the spinel aggregates at the top.

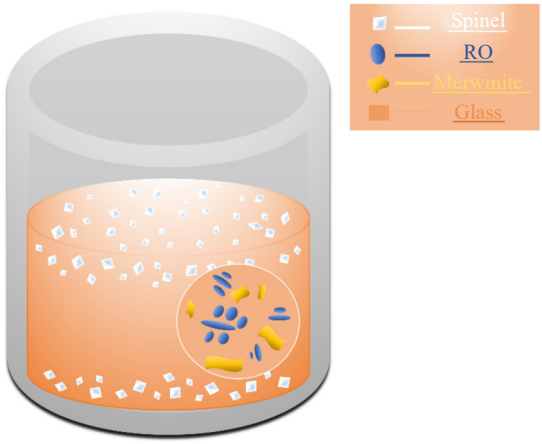

Fig. 5. Schematic pattern of phase space distribution within SSS.

The XRD analysis was afterward performed on the samples quenched with different amounts of FeO, and the results are depicted in Fig. 6, revealing the presence of spinel, glass, merwinite, and RO phases, which agreed with the above SEM–EDS data. Besides, with the increase in FeO doping, the diffraction peak intensity of merwinite gradually decreased, while that associated with spinel remained unchanged. This meant that the presence of FeO in the slag structure inhibited the precipitation of merwinite.

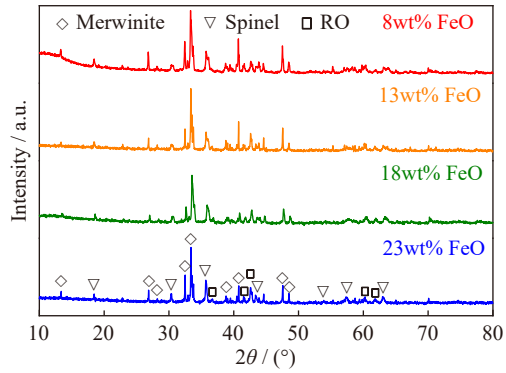

Fig. 6. XRD patterns of water quenched slag samples (1300°C) with different amounts of FeO.

Fig. 7 depicts the SEM–EDS data with the spatial distributions of various phases in the slag after heating at 1600°C. While a tiny amount of spinel phase was distributed at the top of the slag, there were abundant glass and merwinite phases in the middle and a large amount of spinel phase at the bottom of the slag. Through a horizontal comparison of the images in Fig. 7, it was found that when the amount of FeO increased to 18wt%, the spinel phase at the top of the slag increased and more spinel phases were also detected at the bottom of both slag samples.

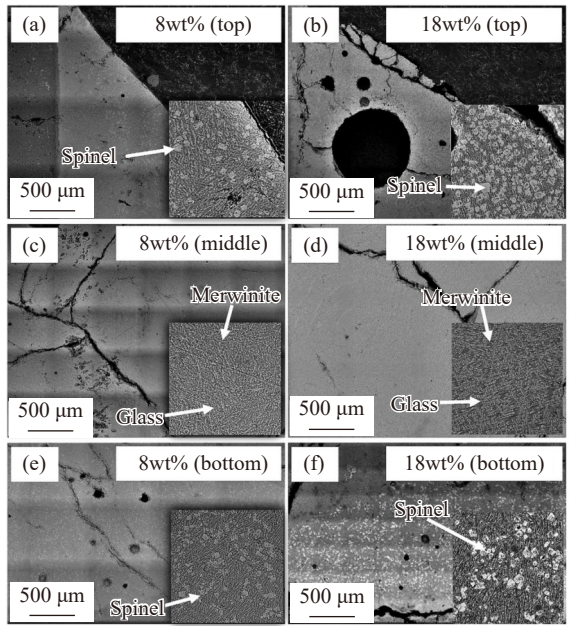

Fig. 7. Splicing SEM images of 1600°C slag samples with 8wt% and 18wt% FeO contents: (a) 8wt% FeO (top), (c) 8wt% FeO (middle), and (e) 8wt% FeO (bottom); (b) 18wt% slag (top), (d) 18wt% slag (middle), and (f) 18wt% slag (bottom).

The XRD results confirmed the phases revealed by EDS. As shown in Fig. S2 the diffraction peak intensity of the spinel phase in the slag sample with 18wt% FeO doping was higher than that at 8wt% FeO, indicating that the addition of FeO was more conducive to the precipitation and growth of

the spinel phase at 1600°C.

Fig. 8 displays the effect of FeO content on the spinel particle size in the slag after heating at 1300°C and water quenching. The results suggested that the average and maximum particle sizes of the spinel precipitated in the slag with 18wt% FeO content were 12.8 and 31.05 μm, respectively, exceeding those of other samples. The minimum size of the precipitated spinel phase was also achieved in the slag sample with 8wt% FeO. As seen from the plots in Fig. 8, at the FeO content less than 18wt%, the spinel size increased with the increasing FeO amount. However, in the sample with 23wt% FeO doping, the average particle size was 12.1 μm and the maximum particle size was 29.2 μm. This result was similar to that of the sample containing 18wt% FeO. Compared with the 18wt% FeO-doped sample, the average particle size of spinel was slightly reduced relative to the maximum size, which indicated that the amount of FeO additive should be controlled within an appropriate range. Above a certain limit, it is no longer conducive to the growth of spinel phase. To further explore this change in particle size, the slag samples with 8wt% and 18wt% FeO contents were water quenched after heating at 1600°C, and their spinel size was then measured. The results showed that the average particle size of the spinel phase in the slag sample with 8wt% FeO was only 5.4 μm. In turn, adding 18wt% FeO made the average particle size of the spinel phase increase to 8.5 μm. At the same time, the results on the slags with 8wt% FeO after water quenching at 1600 and 1300°C revealed that the spinel particle size increased from 5.4 to 7.7 μm with the decrease in heating temperature. Similarly, a comparative analysis of data acquired on slags with 18wt% FeO after the same treatment conditions showed an increase in the spinel size from 8.5 to 12.8 μm. Therefore, not only FeO doping but also the proper control of the cooling mode can promote the efficient growth of the spinel phase. It is worth noting that the same trend in spinel size under controllable cooling conditions was earlier observed in Ref. [33].

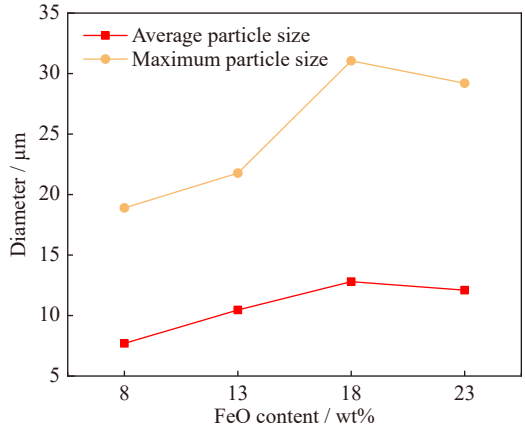

Fig. 8. Relationship between precipitated spinel phase size and FeO content.

The XPS data on valence states of iron in slag sample with 18wt% FeO content quenched in water at 1300°C are shown in Fig. 9. The peaks observed in the Fe 2p spectrum at 711.5 and 725.3 eV were attributed to the spin-orbit splitting of Fe $2p_{3/2}$ and Fe $2p_{1/2}$ states, respectively. Two satellite (sat) peaks at 716.3 and 728.9 eV were ascribed to Fe $2p_{3/2}$ and Fe $2p_{1/2}$ states, respectively [34–35]. The quantitative XPS analysis revealed the presence of divalent and trivalent Fe states with a Fe^{2+}/Fe^{3+} ratio of 41.3/58.7 at 709.6 and 711.9 eV. This indicated that FeO added to the slag was partially oxidized to Fe^{3+} during the melting process, resulting in coexistence of Fe^{2+} and Fe^{3+} in the slag.

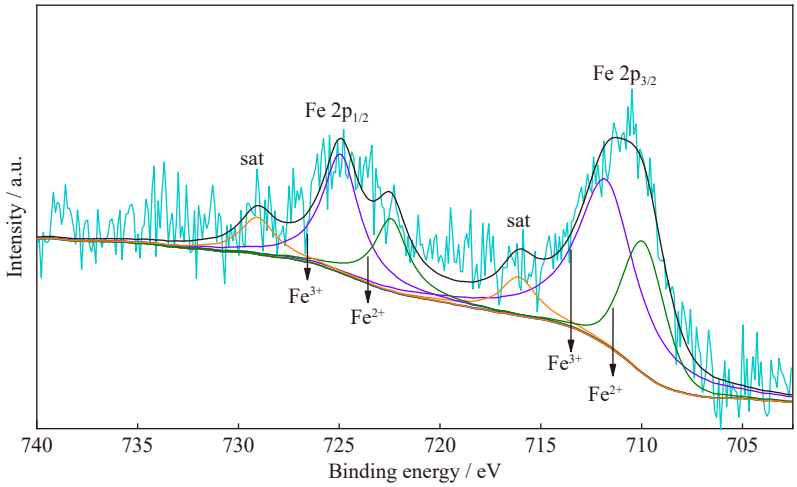

Fig. 9. Analysis of Fe valence states in SSS.

According to the EDS data (Table 3), the iron content in the spinel phase gradually increased with the addition of FeO, which was also the main reason for the increase of the spinel particle size. However, while the atomic percentage of iron gently increased, that of chromium decreased; as a result, the spinel size at 23wt% FeO was slightly inferior to that at 18wt% FeO. This phenomenon is schematically illustrated in Fig. 10. The spinel crystals belonging to the isometric crystal system have a face-centered cubic structure. The tetrahedral and octahedral layers are interspersed, and the number ratio of tetrahedral to octahedral layers is 2:1 [36–37]. The oxygen ions are closely packed in a square so that the trivalent

Table 3. EDS results on spinel phases in slag samples (1300°C) with different FeO contents at%

FeO content / wt%	Ca	Si	Mg	Mn	Al	Fe	Cr	O
8	—	—	11.91	—	4.78	5.71	14.22	63.38
13	—	—	11.14	—	4.67	7.48	13.85	62.86
18	—	—	10.88	—	3.88	8.23	12.70	64.31
23	—	—	11.53	—	4.12	10.18	10.50	63.67

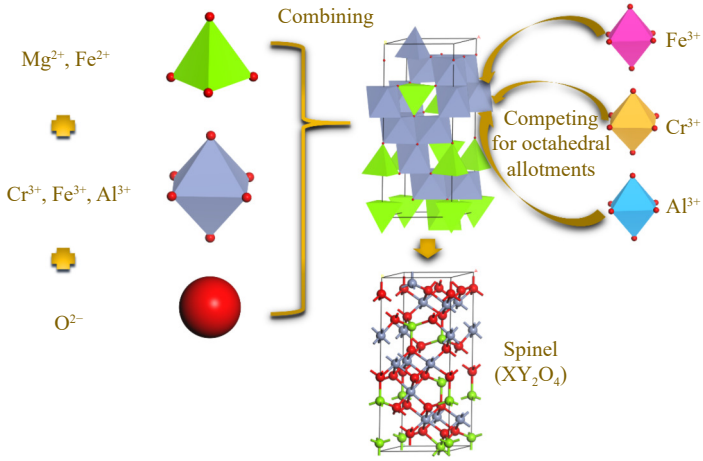

Fig. 10. Interaction between Fe^{3+} and Cr^{3+} during spinel generation.

cations occupy the octahedral voids in six coordinations and the divalent cations occupy the tetrahedral voids in four coordinations. The general formula of the spinel structure is XY_2O_4, in which X and Y are the divalent and trivalent cations occupying the tetrahedral and octahedral positions, respectively [38–39]. In this study, Mg^{2+}, Fe^{2+}, Al^{3+}, Cr^{3+}, Fe^{3+}, and O^{2-} were involved in the production of spinels, and the increase in Fe content in the slag produced Fe^{2+} and Fe^{3+}, both of which contributed positively to a spinel growth. However, Fe^{3+} and Cr^{3+} are in the same octahedral voids, i.e., there is a competitive relationship between them.

According to the above experimental results, properly controlling the cooling system would be conducive to the growth of spinel. The most optimal effect was achieved when using 18wt% FeO as dopant. In addition, compared with other slag samples, that with 23wt% FeO had the highest iron content in the spinel phase. The increase of iron content combined with the spatial distribution of SSS can exert a positive impact on the recovery of chromium resources in the slag via magnetic separation [40].

3.3. Action mechanism of FeO

To study the action mechanism of FeO, the prepared FeO lump was put into the slag sample S1, which was completely melted at 1600°C. After 1 min of the reaction, the obtained system was rapidly cooled to room temperature. Fig. 11 displays the SEM images of the interface zone between the FeO lump and the slag, and the schematic of the FeO action on the slag is illustrated in Fig. 12. The elements of each phase were analyzed via EDS. As shown in Fig. 11(a), three areas could be distinguished based on the EDS data as follows: (1) a FeO-rich area on the upper side, (2) a molten area on the lower side, and (3) a reaction interface area in the middle. Fig. 11(b) depicts the magnified (2000×) SEM image of the transition area between the FeO-rich area and the reaction interface area. As seen from the image, the FeO lump was melted in 1 min, exhibiting plenty of droplets. According to the EDS analysis, some metallic elements, such as calcium, magnesium, manganese, silicon, and chromium, entered the FeO droplets. The surrounding phases of glass and merwinite increased the iron content. The molten droplets formed after the melting of FeO in the reaction interface region caused the emergence of RO phase with the entry of mag-

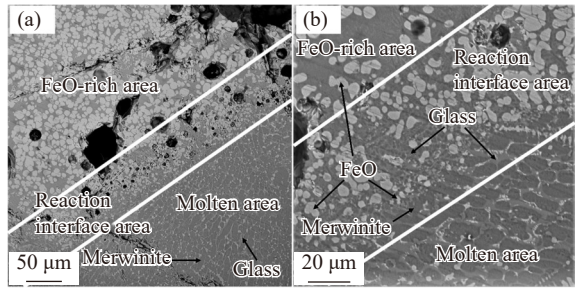

Fig. 11. (a) SEM image of the interface area between FeO briquette quenched at 1600°C and S1 slag and (b) the magnified (2000×) SEM image.

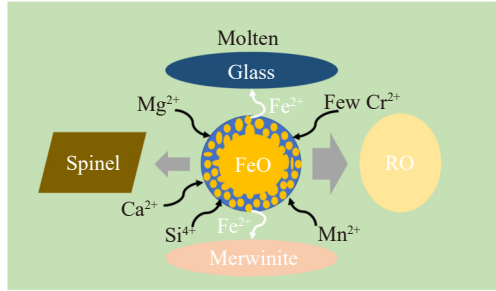

Fig. 12. Illustration of FeO action mechanism in SSS.

nesium, manganese, and other elements. Since a small amount of chromium penetrated into the RO phase, it was easily dissolved due to its instability in the aqueous solution, causing environmental pollution. Therefore, the amount of FeO added to SSS should be controlled within an appropriate range.

As shown in Fig. 11(b), the FeO droplets gradually decreased as they approached the reaction interface until completely disappearing. Since FeO blocks were added to the slag from the top layer, they were only partially integrated into the slag after quenching for 1 min and were still present on the surface of the slag. This meant that the reaction interface was located on the upper surface of the slag. After quenching at 1300°C, the spinel phase was distributed at the top and bottom of slag, while it was concentrated at the bottom at 1600°C. For this reason, no spinel was identified at the reaction interface in Fig. 11. Furthermore, the merwinite phase in the FeO-rich region was free of chromium, whereas some chromium elements were detected in the glass phase across the interfacial region.

In summary, the mechanism of action of FeO on SSS in the current study can be proposed as follows. In the first stage, a solid FeO phase gradually melts and forms droplets which are then dissolved in the molten slag. During this process, the slag viscosity and the liquid temperature decrease [41], which improves the crystallization kinetics of slag precipitation. It is noteworthy that a similar behavior was also observed by Zhao *et al.* [42] after adding MnO. In the second stage, some chromium elements in the surrounding phases travel toward the RO phase formed by FeO melting, which affects their distribution behavior. Finally, the high compatibility of Fe^{2+} and spinel structure is conducive to the crystallization and growth of spinel [43].

4. Conclusions

(1) The addition of FeO to SSS could improve the spinel phase growth compared to slags with Fe_2O_3 and Fe_3O_4 or without any iron oxide. During quenching after heating at 1300°C, the most optimal structural parameters were achieved in the experimental slag sample with the 18wt% FeO content. The average particle size of the spinel was 12.8 μm and the maximum particle size was 31.05 μm.

(2) The phases were spatially distributed throughout the slag. The spinel phase was mainly localized at the top and bottom of the slag. The middle part was predominately made of glass and RO phases, and the matrix phase was composed of merwinite. With the increase of FeO content from 8wt% to 23wt%, the spinel phase gradually moved from the bottom to the top of the slag. The most optimal effect was obtained in the slag with 18wt% FeO doping.

(3) The average and maximum particle sizes of the spinel phase in the slag with 18wt% FeO were larger than those in slags with FeO contents of 8wt%–23wt% (except for 18wt%). The average size of spinel in the slag with 23wt% FeO was 12.1 μm and the maximum size was 29.2 μm. These trends were similar to those of the 18wt% FeO-doped slag, exhibiting a slight reduction in the corresponding values.

Acknowledgements

The authors gratefully acknowledge supports by the National Natural Science Foundation of China (Nos. 52074078 and 52374327), the Applied Fundamental Research Program of Liaoning Province (No. 2023JH2/101600002), the Shenyang Young Middle-Aged Scientific and Technological Innovation Talent Support Program (No. RC220491), the Liaoning Province Steel Industry-University-Research Innovation Alliance Cooperation Project of Bensteel Group (No. KJBLM202202), and the Fundamental Research Funds for the Central Universities (Nos. N2201023 and N2325009).

Conflict of Interest

All authors declare no competing financial interest.

Supplementary Information

The online version contains supplementary material available at https://doi.org/10.1007/s12613-023-2713-7.

References

[1] Q. Zhao, C.J. Liu, X.H. Mei, H. Saxén, and R. Zevenhoven, Research progress of steel slag-based carbon sequestration, *Fundam. Res.*, 2022. https://doi.org/10.1016/j.fmre.2022.09.023

[2] J. Xiong, Y.L. Tong, J.L. Peng, and S.H. Zhang, Strength–toughness improvement of 13Cr4NiMo martensitic stainless steel with thermal cyclic heat treatment, *J. Iron Steel Res. Int.*, 30(2023), No. 8, p. 1499.

[3] C.Q. Wang, J. Li, H. Yang, and C.R. Li, Feasibility analysis of industrial waste acid treatment of stainless steel smelting slag, *Mod. Metall.*, 38(2010), No. 1, p. 1.

[4] X. Zhang, M. Zhang, and M. Guo, Advances and trends in high-temperature modification–crystallization control detoxification of stainless steel slag, *Chin. J. Eng.*, 45(2023), No. 4, p. 577.

[5] L.H. Cao, C.J. Liu, Q. Zhao, and M.F. Jiang, Analysis on the stability of chromium in mineral phases in stainless steel slag, *Metall. Res. Technol.*, 115(2018), No. 1, art. No. 114.

[6] Y.M. Li, Q. Zhao, X.H. Mei, C.J. Liu, H. Saxén, and R. Zevenhoven, Effect of Ca/Mg molar ratio on the calcium-based sorbents, *Int. J. Miner. Metall. Mater.*, 30(2023), No. 11, p. 2182.

[7] K. Pillay, H. von Blottnitz, and J. Petersen, Ageing of chromium(III)-bearing slag and its relation to the atmospheric oxidation of solid chromium(III)-oxide in the presence of calcium oxide, *Chemosphere*, 52(2003), No. 10, p. 1771.

[8] W.L. Li and X.X Xue, Effect of cooling regime on phase transformation and chromium enrichment in stainless-steel slag, *Ironmaking Steelmaking*, 46(2019), No. 7, p. 642.

[9] Q. Zhao, K. Liu, L.F. Sun, *et al.*, Towards carbon sequestration using stainless steel slag via phase modification and co-extraction of calcium and magnesium, *Process. Saf. Environ. Prot.*, 133(2020), p. 73.

[10] Q.Q. Mou, J.L. Li, Q. Zeng, and H.Y. Zhu, Effect of Fe_2O_3 on the size and components of spinel crystals in the $CaO–SiO_2–MgO–Al_2O_3–Cr_2O_3$ system, *Int. J. Miner. Metall. Mater.*, 26(2019), No. 9, p. 1113.

[11] H.T. Shen and E. Forssberg, An overview of recovery of metals

from slags, *Waste Manage.*, 23(2003), No. 10, p. 933.
[12] F. Kukurugya, P. Nielsen, and L. Horckmans, Up-concentration of chromium in stainless steel slag and ferrochromium slags by magnetic and gravity separation, *Minerals*, 10(2020), No. 10, art. No. 906.
[13] M. Tossavainen, F. Engstrom, Q. Yang, *et al*., Characteristics of steel slag under different cooling conditions, *Waste Manage.*, 27(2007), No. 10, p. 1335.
[14] F. Engström, D. Adolfsson, Q. Yang, C. Samuelsson, and B. Björkman, Crystallization behaviour of some steelmaking slags, *Steel Res. Int.*, 81(2010), No. 5, p. 362.
[15] Z.J. Wang and I. Sohn, Understanding the solidification and leaching behavior of synthesized Cr-containing stainless steel slags with varying Al_2O_3/SiO_2 mass ratios, *Ceram. Int.*, 47(2021), No. 8, p. 10918.
[16] Z.J. Wang and I. Sohn, Immobilizing chromium in stainless steel slags with MnO addition, *J. Am. Ceram. Soc.*, 104(2021), No. 2, p. 697.
[17] Y.M. Zhang, L.Y. Yi, L.N. Wang, *et al*., A novel process for the recovery of iron, titanium, and vanadium from vanadium-bearing titanomagnetite: Sodium modification–direct reduction coupled process, *Int. J. Miner. Metall. Mater.*, 24(2017), No. 5, p. 504.
[18] S.K. Das, Quantitative mineralogical characterization of chrome ore beneficiation plant tailing and its beneficiated products, *Int. J. Miner. Metall. Mater.*, 22(2015), No. 4, p. 335.
[19] Q. Zhao, J.Y. Li, K.W. You, and C.J. Liu, Recovery of calcium and magnesium bearing phases from iron–and steelmaking slag for CO_2 sequestration, *Process. Saf. Environ. Prot.*, 135(2020), p. 81.
[20] L.H. Cao, C.J. Liu, Q. Zhao, and M.F. Jiang, Effect of Al_2O_3 modification on enrichment and stabilization of chromium in stainless steel slag, *J. Iron Steel Res. Int.*, 24(2017), No. 3, p. 258.
[21] L. Holappa, M. Kekkonen, A. Jokilaakso, and J. Koskinen, A review of circular economy prospects for stainless steelmaking slags, *J. Sustain. Metall.*, 7(2021), No. 3, p. 806.
[22] L. Liu, M.L. Hu, C.G. Bai, X.W. Lü, Y.Z. Xu, and Q.Y. Deng, Effect of cooling rate on the crystallization behavior of perovskite in high titanium-bearing blast furnace slag, *Int. J. Miner. Metall. Mater.*, 21(2014), No. 11, p. 1052.
[23] Q. Zhao, C.J. Liu, L.H. Cao, *et al*., Shear-force based stainless steel slag modification for chromium immobilization, *ISIJ Int.*, 59(2019), No. 3, p. 583.
[24] X.R. Wu, X.M. Dong, R.T. Wang, H.H. Lu, F.B. Cao, and X.M. Shen, Crystallization behaviour of chromium in stainless steel slag: Effect of feo and basicity, *J. Residuals Sci. Technol.*, 13(2016), Suppl. 1, p. S57.
[25] T.X. Yu, T. Jiang, J. Wen, H.Y. Sun, M. Li, and Y. Peng, Effect of chemical composition on the element distribution, phase composition and calcification roasting process of vanadium slag, *Int. J. Miner. Metall. Mater.*, 29(2022), No. 12, p. 2144.
[26] S. Zhang, Y.L. Zhang, and S.W. Wu, Effects of ZnO, FeO and Fe_2O_3 on the spinel formation, microstructure and physico-chemical properties of augite-based glass ceramics, *Int. J. Miner. Metall. Mater.*, 30(2023), No. 6, p. 1207.
[27] Q. Zeng, J.L. Li, Q.Q. Mou, H.Y. Zhu, and Z.L. Xue, Effect of FeO on spinel crystallization and chromium stability in stainless steel-making slag, *JOM*, 71(2019), No. 7, p. 2331.
[28] Z.J. Wang and I. Sohn, Selective elemental concentration during the solidification of stainless steel slags for increased Cr recovery with MnO addition, *J. Am. Ceram. Soc.*, 103(2020), No. 10, p. 6012.
[29] Z.J. Wang, J. Yang, D.A. Pan, B. Liu, J.J. Tian, and S.G. Zhang, Present state of stainless steel slag resources disposal technique, *J. Iron Steel Res.*, 27(2015), No. 2, p. 1.
[30] J. Diao, B. Xie, Y. Wang, and C.Q. Ji, Mineralogical characterisation of vanadium slag under different treatment conditions, *Ironmaking Steelmaking*, 36(2009), No. 6, p. 476.
[31] S.W. Wu, Y.L. Zhang, and S. Zhang, Chromium enrichment in different crystalline phases of Cr-containing slag under various basicities and equilibrium temperatures, *J. Iron Steel Res. Int.*, 29(2022), No. 9, p. 1412.
[32] X. Lu, X.L. Huang, R.F. Wei, *et al*., Novel method for improving iron recovery from electric arc furnace slag: On-site hot modification, *J. Iron Steel Res. Int.*, 29(2022), No. 8, p. 1224.
[33] Q. Zhao, C.J. Liu, L.H. Cao, X. Zheng, and M.F. Jiang, Stability of chromium in stainless steel slag during cooling, *Minerals*, 8(2018), No. 10, art. No. 445.
[34] T.X. Nguyen, J. Patra, J.K. Chang, and J.M. Ting, High entropy spinel oxide nanoparticles for superior lithiation–delithiation performance, *J. Mater. Chem. A*, 8(2020), No. 36, p. 18963.
[35] K.H. Tian, C.Q. Duan, Q. Ma, *et al*., High-entropy chemistry stabilizing spinel oxide $(CoNiZnXMnLi)_3O_4$ (X = Fe, Cr) for high-performance anode of Li-ion batteries, *Rare Met.*, 41(2022), No. 4, p. 1265.
[36] H.F. Shang and D.G. Xia, Spinel $LiMn_2O_4$ integrated with coating and doping by Sn self-segregation, *Int. J. Miner. Metall. Mater.*, 29(2022), No. 5, p. 909.
[37] F. Yuan, Z. Zhao, Y.L. Zhang, and T. Wu, Effect of Al_2O_3 content on the viscosity and structure of $CaO–SiO_2–Cr_2O_3–Al_2O_3$ slags, *Int. J. Miner. Metall. Mater.*, 29(2022), No. 8, p. 1522.
[38] W.S. Dong, X.K. Wang, and S.Y. Peng, Preparation properties and use in catalysis of spinels, *J. Petrochem. Univ. Sinopec*, 9(1996), No. 4, p. 10.
[39] Z.Y. Tang, J.J. Feng, and G.X. Xu, Study on multiple doping of spinel $LiMn_2O_4$, *Acta Chim. Sin.*, 61(2003), No. 8, p. 1316.
[40] Q. Zhao, C.J. Liu, B. Zhang, M.F. Jiang, J. Qi, H. Saxén, and R. Zevenhoven, Study on extraction of iron from chromite, *Steel Res. Int.*, 86(2015), No. 12, p. 1541.
[41] Y.Z. Huo, H.Z. Gu, A. Huang, *et al*., Characterization and mechanism of dissolution behavior of Al_2O_3/MgO oxides in molten slags, *J. Iron Steel Res. Int.*, 29(2022), No. 11, p. 1711.
[42] Q. Zhao, C.J. Liu, T.C. Gao, L. Gao, H. Saxén, and R. Zevenhoven, Remediation of stainless steel slag with MnO for CO_2 mineralization, *Process. Saf. Environ. Prot.*, 127(2019), p. 1.
[43] J.L. Li, A.J. Xu, D.F. He, Q.X. Yang, and N.Y. Tian, Effect of FeO on the formation of spinel phases and chromium distribution in the $CaO–SiO_2–MgO–Al_2O_3–Cr_2O_3$ system, *Int. J. Miner. Metall. Mater.*, 20(2013), No. 3, p. 253.